Generation of Tightly Focused Cylindrical Vector Beams with Dual-Channel Transmissive Metasurfaces

Jialin Feng ⬤,[1] Hongyu Shi, Dr.,[1,*] Jianjia Yi,[2] Anxue Zhang,[2] Shah Nawaz Burokur,[3] Juan Chen,[4] Xiaoming Chen,[4] and Zhuo Xu[5]

[1] *Ministry of Education Key Laboratory for Multifunctional Materials and Structures, Xi'an Jiaotong University, Xi'an 710049, China*

[2] *School of Electronic and Information Engineering, Xi'an Jiaotong University, Xi'an 710049, China*

[3] *LEME, UPL, Université Paris Nanterre, Ville d'Avray F92410, France*

[4] *School of Information and Communications Engineering, Xi'an Jiaotong University, Xi'an 710049, China*

[5] *The Electronic Materials Research Laboratory, Key Laboratory of the Ministry of Education, Xi'an Jiaotong University, Xi'an 710049, China*

Tightly focusing cylindrical vector beams (CVBs) are widely used in diverse applications from particle trapping to high-resolution microscopy. Recently, planar metasurfaces have been proposed as promising alternatives to traditional bulky optical devices for tightly focused CVB generation. However, few metasurfaces allow the generation and independent phase control of different CVBs. In this paper, cascaded dual-channel transmissive metasurfaces that can be used to simultaneously generate different CVBs and independently control their phases are designed. The polarization and phase of the transmitted waves are controlled independently via only two geometric parameters. Under x- and y-polarized wave incidences, the radially polarized beam (RPB) and azimuthally polarized beam (APB) are generated by a first metasurface. In addition, a second metasurface is used to produce different focal fields in different focal planes under RPB and APB excitations. In such a proposed approach, the phase responses of the RPB and APB are distinct, which is significantly different from existing designs. A regular polygonlike focus and a lateral displacement of the focal spot are, respectively, realized in different focal planes at 7.8 GHz through different channels. Our approach improves the flexibility of focusing, allowing the generation of focal arrays at different locations within the same focal plane. Since the electromagnetic energy can be confined to a small specific zone in the microwave band, the proposed method can provide the basis for a number of important applications in the medical domain, such as the accurate hyperthermia treatment of large area tumors.

I. INTRODUCTION

Traditional polarization manipulation usually involves beams with homogeneous polarization distributions, such as linear, elliptical, and circular polarizations. Recently, vector beams with spatially inhomogeneous polarization states have begun to be widely investigated due to the additional degrees of freedom that they provide for wave manipulation [1]. As a special type of such beams, cylindrical vector beams (CVBs) have axial symmetry in both amplitude and phase [2]. CVBs have attracted intensive research interest due to their unique properties in tight focusing scenarios, which are different from beams with a spatially homogeneous polarization distribution. For example, the focal spot of a tightly focused radially polarized beam (RPB) is significantly smaller than that of

a linearly polarized beam since the former is dominated by longitudinal field components. Because of their specific tightly focusing characteristics, CVBs have been applied in high-resolution imaging [3], plasmon excitation [4], and communication systems [5]. In addition, a large variety of focal fields with different strengths and polarization distributions can be generated under tightly focusing conditions [6–9].

Traditional approaches for CVB generation include active and passive methods. Approaches of the former type commonly involve the use of lasers with specially designed components to force the electromagnetic (EM) waves to oscillate in a circularly symmetric polarization mode [10,11]. These methods allow the efficient generation of CVBs but the types of output CVBs are limited and only a specific CVB can be obtained each time. Passive schemes mainly use devices with spatially varying polarization characteristics such as spatial light modulators

---

[12,13] and subwavelength gratings [14] to convert a beam with a homogeneous polarization state to a CVB. In addition, these methods also contain components such as wave plates and lenses. For example, Chen *et al.* proposed a method for generating CVBs via the interference superposition of two beams in a 4-*f* system [15]. Although these conventional methods successfully demonstrate the generation of CVBs, they usually require bulky optical devices and the possibilities of device miniaturization and integration in other systems are severely limited. Moreover, the modulation of CVBs is needed in some practical applications. For instance, the tight focusing of a CVB is usually realized with additional lenses, which further increases the complexity of these systems.

Metasurfaces, which are two-dimensional (2D) versions of metamaterials, are composed of periodic subwavelength artificial structures with an unprecedented ability to control the polarization, phase, amplitude, and frequency of EM waves [16]. In addition, metasurfaces exhibit the advantages of low profile, low loss, and a relative ease of fabrication, while allowing wave modulation and facilitating the integration of optical systems. By manipulating the polarization, phase, and amplitude of light, several functions have been realized using metasurfaces, such as Bessel beam generation [17], vortex beam generation [18], holography [19], polarization conversion [20], and focusing [21]. Because of their powerful capability to modulate EM waves, metasurfaces have been proposed to generate different CVBs [22–27], including RPBs, azimuthally polarized beams (APBs), and vector vortex beams.

Recently, metasurfaces capable of both generating and modulating CVBs have been reported. A radially polarized Lorentz beam capable of performing CVB amplitude modulation has been achieved at terahertz frequencies with a single-layer metasurface [28]. Metasurfaces have also been designed to both generate and tightly focus a RPB, with a sharp focus spot obtained in the focal plane [29,30], but their operation is limited to *x*-polarized wave excitation and, consequently, the designs are not flexible for dual-polarization applications. In Refs. [31,32] dual-polarized metasurfaces have been proposed to simultaneously generate and tightly focus a RPB and APB under orthogonal linearly polarized wave illuminations. However, the constituting meta-atom is designed as a half-wave plate, and the phase responses of the RPB and APB are identical, which does not allow independent modulation. Therefore, these designs cannot be used to achieve different focal fields with different phase responses of the RPB and APB. In addition, the phase tuning in these metasurfaces is realized by the tailoring of the shapes and dimensions of each meta-atom, which usually requires simultaneous optimizations of several geometric parameters, making it almost impossible to modulate the transmitted waves phase continuously. A multilayer metasurface allowing full control over phase, amplitude, and the polarization state of light

by manipulating the complex amplitude of the orthogonal polarization states has been proposed [33]. However, its phase regulation method is complex and similar to the designs reported in Refs. [31,32]. A transmissive geometric metasurface with independent complex-amplitude modulations of EM waves at two frequencies has been proposed [34], but only operates for circularly polarized (CP) waves. In addition, most of the mentioned metasurfaces can tightly focus CVBs at optical or terahertz regimes, which limits their applications at lower frequencies. For instance, microwave hyperthermia, an emerging cancer treatment technique, requires an accurately focused beam to heat the tumor tissues rather than healthy tissues [35–38]. However, although a few metasurfaces generating CVBs in the microwave band have been proposed [39,40], these designs simply deal with the generation of CVBs and do not allow further modulation, which hinders their practical adoption in such real-life applications. Therefore, designing dual-channel metasurfaces that can generate different CVBs and simultaneously produce different focal fields under tightly focusing conditions presents significant challenges in the microwave band.

Herein, a dual-channel coupling-propagation-decoupling (CPD) meta-atom is proposed to simultaneously and independently modulate the polarization and phase of two orthogonal linearly polarized incident waves. The polarization and phase of the transmitted waves are independently controlled through two geometric parameters. Then, utilizing the proposed CPD meta-atoms, a first dual-channel metasurface is designed to generate a RPB and APB at 7.8 GHz under *x*- and *y*-polarized incidence, respectively. A second dual-polarized metasurface is designed to operate as a combination of a lens and a phase diffractive optical element (DOE), which can modulate the phase of a RPB and APB independently. Finally, the two dual-channel metasurfaces are cascaded to realize a regular polygonlike flat-top focus and a lateral displacement of the focal spot in different focal planes through two channels under tightly focusing conditions. Most importantly, our design is not based on the half-wave plate as in previous reported studies [31,32]. By introducing a double-layer stripline structure in designed meta-atoms, we successfully overcome the drawback of not being able to adjust the APB and RPB phases independently. The proposed method paves a new way for generating complex vector beams and focal fields, which have great potential in microwave applications such as hyperthermia treatment.

II. DESIGN AND DEMONSTRATION OF METASURFACES FOR CVB GENERATION AND MANIPULATION

A schematic illustration of the dual-channel transmissive metasurfaces that generate and tightly focus the different CVBs at 7.8 GHz is shown in Fig. 1. The first metasurface (MS1) is illuminated by a linearly polarized plane
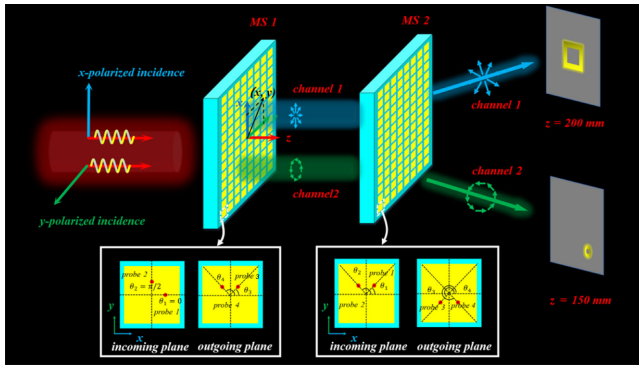
FIG. 1. Schematic diagram of the dual-channel transmissive metasurface that generates and tightly focuses azimuthally and radially polarized beams from incident x- and y-polarized beams, respectively. The insets shows the information about the azimuth angles of four probes of meta-atom as θ_1, θ_2, θ_3, and θ_4, respectively. In order to generate RPB and APB through the two channels under x- and y-polarized wave illuminations, the θ_1, θ_2, θ_3, and θ_4 of the meta-atoms for MS1 are chosen as $\theta_1 = 0$, $\theta_2 = \pi/2$, $\theta_3 = \arctan(y/x)$, and $\theta_4 = \arctan(y/x) + \pi/2$. To independently modulate the generated APB and RPB, the θ_1, θ_2, θ_3, and θ_4 of the MS2 meta-atom are set to $\theta_1 = \arctan(y/x)$, $\theta_2 = \arctan(y/x) + \pi/2$, $\theta_3 = \theta_1 + \pi$, $\theta_4 = \theta_2 + \pi$, respectively.

wave propagating along the z direction. After modulation by MS1, the polarization of the output wave becomes radial or angular when excited by x- or y-polarized waves, respectively. The second metasurface (MS2) can modulate the transmission phase of the RPB and APB independently, and can be considered as a component that combines a lens and a phase DOE. Based on the tightly focusing properties of the CVBs, the regular-polygon-like focus and lateral displacement of the focal spot are realized in different focal planes ($z = 200$ mm and $z = 150$ mm) through two channels when MS2 is illuminated by a RPB and APB, respectively.

A. Design of constituting dual-channel meta-atom

Figures 2(a) and 2(b) show the structure of the designed dual-channel meta-atom, which comprises of six layers of metallic patterns with a thickness of 0.035 mm: top layer, ground layer 1, line 1, line 2, ground layer 2, and bottom layer. Five layers of Rogers 4350B substrates (labeled sub 1–5) with a dielectric constant $\epsilon_r = 3.55$ and a loss tangent $\tan \delta = 0.0037$, are used to separate the metallic patterns. Their thicknesses are h_1, h_2, h_3, h_4, and h_5, as shown in Fig. 2(a). The designed dual-channel meta-atom has a period P. The top and bottom layers are square dual-polarized patches with length P_1, which are used to receive and transmit EM waves, respectively. Ground layers 1 and 2, and lines 1 and 2 form two striplines for the designed dual-channel meta-atom. Lines 1 and 2 (with lengths L_1/L_2 and a width w) guide the received EM waves and convert them to arbitrarily polarized transmitted waves. In addition, lines

1 and 2 can also offer independent and linear phase delays for the two channels. To avoid interference between the two channels caused by the overlap of lines 1 and 2, sub 3 is used to separate them. Four probes with a radius r_i are marked using red circles in Fig. 2(b), and their positions are (fx_1, fy_1), (fx_2, fy_2), (fx_3, fy_3), and (fx_4, fy_4), respectively, while their corresponding azimuth angles are θ_1, θ_2, θ_3, and θ_4. Ground layers 1 and 2 have two holes of radius r_0 at the locations of the probes to avoid short circuiting them. The designed meta-atom is a dual-channel device, where probe 1 (probe 2) and probe 3 (probe 4) are connected by line 1 (line 2) to form channel 1 (channel 2). For channel 1 (channel 2), probe 1 (probe 2) and probe 3 (probe 4) connect the top layer, line 1 (line 2) and the bottom patch. $\theta_1 (\theta_2)$ ensures that the top patch can receive the θ_1-polarized (θ_2-polarized) wave into the channel 1 (channel 2). Angle $\theta_3 (\theta_4)$ determines that the bottom patch can transmit the θ_3-polarized (θ_4-polarized) wave to the free space through channel 1 (channel 2). Figures 2(c) and 2(d) show the E-field distributions of the meta-atom when $\theta_1 = 0$, $\theta_2 = \pi/2$, $\theta_3 = 3\pi/2$, and $\theta_4 = \pi$ and excited by x- and y-polarized waves, respectively. For channel 1, when an x-polarized incident EM wave illuminates the meta-atom along the z direction, the top patch couples the incoming EM wave to line 1 through probe 1 and we can observe from Fig. 2(c) that the tangential E-field excites the propagation mode in line 1. Then, the EM wave is delayed and transmitted to the bottom layer through probe 3. Eventually, the bottom layer decouples the EM wave into a space wave propagation with y polarization. Figure 2(d) shows the E-field distribution when channel 2 of the meta-atom is excited by a y-polarized wave. It can be observed that the polarization of the transmitted wave becomes x polarized. The E-field distribution around line 2 and line 1 is similar, which means that the propagation mode of line 2 is excited in this case. Without loss of generality, the values of $\theta_1 (\theta_2)$ and $\theta_3 (\theta_4)$ can be chosen freely to achieve arbitrary linear polarization conversion. However, to avoid the polarization coupling between the two channels, which would severely decrease their isolation, the azimuth angles of four probes satisfy

$$\theta_2 = \theta_1 + \pi/2, \quad \theta_4 = \theta_3 + \pi/2. \tag{1}$$

To summarize, the designed dual-channel meta-atom can achieve a linear polarization conversion of θ_1 to θ_3 (θ_2 to θ_4) through channel 1 (channel 2).

To maximize transmittance of the designed dual-channel meta-atom, impedance matching between line 1 (line 2), top and bottom patches is necessary. The width w of line 1 (line 2) and the distance R from the four probes to the center of the designed meta-atom are set to 0.5 and 2.3 mm, respectively, to achieve a good impedance matching for channel 1 (channel 2). The four probes of the meta-atom

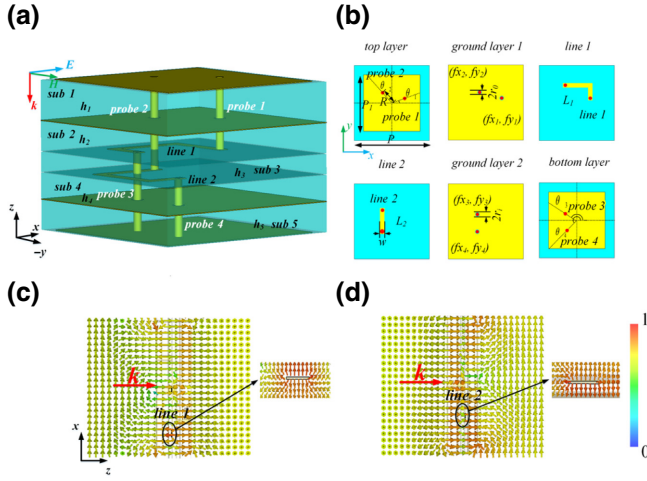**(a)**

(b)

(c)

(d)

FIG. 2. (a) Schematic diagram of the meta-atom. (b) Close view of the six metal patterns of the meta-atom. The dimensions of the meta-atom are $P = 10$ mm, $P_1 = 9$ mm, $w = 0.5$ mm, $r_0 = 0.3$ mm, $r_i = 0.2$ mm, $h_1 = 0.76$ mm, $h_2 = 0.2$ mm, $h_3 = 0.25$ mm, $h_4 = 0.2$ mm, $h_5 = 0.71$ mm, $L_1 = 8$ mm, $L_2 = 8$ mm, $R = 2.3$ mm. The values of $fx_1, fy_1, fx_2, fy_2, fx_3, fy_3, fx_4$, and fy_4 vary according to $\theta_1, \theta_2, \theta_3$, and θ_4. (c) The E-field distribution of the meta-atom for channel 1 when $\theta_1 = 0, \theta_2 = \pi/2, \theta_3 = 3\pi/2$, and $\theta_4 = \pi$ and excited by an x-polarized wave. (d) The E-field distribution of the meta-atom for channel 2 when $\theta_1 = 0$, $\theta_2 = \pi/2, \theta_3 = 3\pi/2$, and $\theta_4 = \pi$ and excited by a y-polarized wave.

then satisfy the condition

$$\sqrt{fx_i^2 + fy_i^2} = R \quad (i = 1, 2, 3, 4), \qquad (2)$$

$$fx_i = R * \cos(\theta_i), \quad fy_i = R * \sin(\theta_i) \quad (i = 1, 2, 3, 4). \qquad (3)$$

Hence, the four probes vary on a circle of radius $R = 2.3$ mm to maintain a good impedance matching between the top patch, the stripline, and the bottom patch. The length of line 1 (line 2) can modulate the transmission phase delay of the θ_3-polarized (θ_4-polarized) wave in channel 1 (channel 2). Unlike previous metasurface designs, whose phase modulation usually involves the optimization of several geometric parameters [29–32], the transmission phase of the θ_3-polarized (θ_4-polarized) wave can be adjusted linearly by changing the length of line 1 (line 2). The guided wavelength of the stripline can be expressed as

$$\lambda_g = \lambda_0/\sqrt{\epsilon_r}, \qquad (4)$$

where $\lambda_0 = c/f_0$ represents the wavelength of EM waves in free space, $f_0 = 7.8$ GHz is the operation frequency, and the guided wavelength of the stripline is $\lambda_g = 20.5$ mm.

The variation of the length ΔL_1 (ΔL_2) of line 1 (line 2) results in a phase change of $2\pi * \Delta L_1/\lambda_g$ ($2\pi * \Delta L_2/\lambda_g$). Thus, a phase change up to $360°$ in channel 1 (channel 2) can be achieved when ΔL_1 (ΔL_2) varies within 20.5 mm. In conclusion, the designed dual-channel meta-atom can simultaneously and independently modulate the polarization and phase of two orthogonal linearly polarized incident waves.

B. Metasurfaces for generating and modulating CVBs

To generate a RPB and APB through the two channels under different linearly polarized wave illuminations, each meta-atom of MS1 should be able to arbitrarily control the polarization of the transmitted waves while ensuring an identical phase of the transmitted waves to achieve a normal forward beam. According to the analysis in Sec. II A, θ_1 and θ_2 of the meta-atoms for MS1 are chosen as $\theta_1 = 0$ and $\theta_2 = \pi/2$ to ensure that the top patch can independently receive x-polarized and y-polarized waves. We define the polarization angle of the transmitted waves as $0°$ when it is along the $+x$ direction. To obtain the ideal RPB (APB) through channel 1 (channel 2) when the MS1 is illuminated by x-polarized (y-polarized) waves, θ_3 and θ_4 of each MS1 meta-atom are $\theta_3 = \arctan(y/x)$ and $\theta_4 = \arctan(y/x) + \pi/2$, respectively, according to the polarization states of the RPB and APB. Here, (x, y) is the location of each meta-atom on the MS1 as shown in Fig. 1. On the other hand, the transmission phase of all MS1 meta-atoms should be identical. Thus, L_1 (L_2) of each MS1 meta-atom should be equal to ensure that they have identical transmission phases in channel 1 (channel 2) to produce a forward RPB (APB).

The elementary meta-atoms of MS1 are simulated using the commercial simulation software CST Microwave Studio. The transmittance T is plotted in Fig. 3(a) for θ_3 values of $30°$, $45°$, and $60°$ for the MS1 meta-atoms while illuminated by an x-polarized incidence, and Fig. 3(b) shows the transmittances of MS1 meta-atoms for θ_4 values of $120°$, $135°$, and $150°$ under a y-polarized wave illumination. In Figs. 3(a) and 3(b) the numbers inside the parentheses denote the polarization angle of the transmitted waves, and x and y in the subscript represent x- and y-polarized excitation, respectively. As shown in Figs. 3(a) and 3(b), the amplitudes of the θ_3-polarized and θ_4-polarized transmitted waves remain above 0.9 at 7.8 GHz, which indicates that the designed meta-atom of MS1 can achieve arbitrary linear polarization conversion in channel 1 (channel 2) under x-polarized (y-polarized) wave illumination efficiently. To independently modulate the generated APB and RPB, MS2 must be capable of independently modulating the phase of the two channels. Although the designed meta-atom can simultaneously and independently modulate the phase and polarization of the transmitted waves, only phase manipulation is required to tightly focus CVBs. Based on
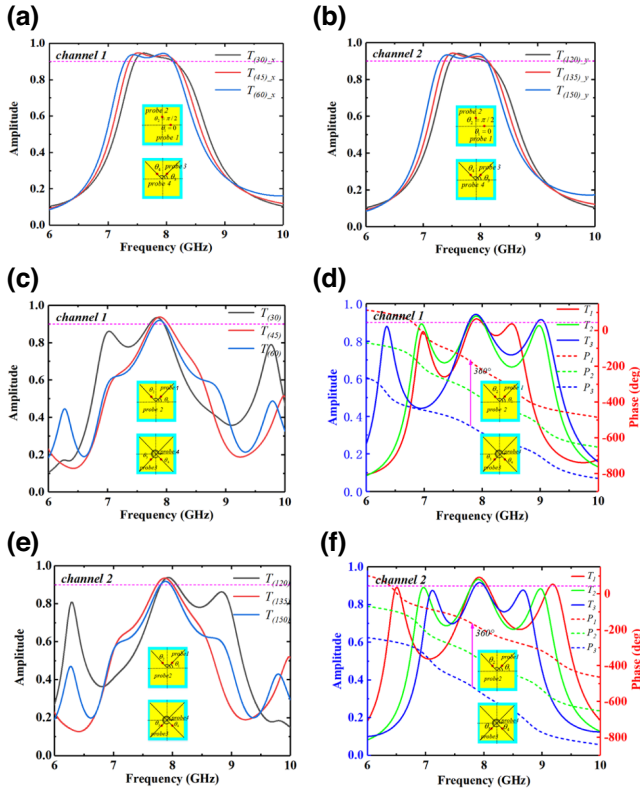
FIG. 3. (a) Simulated transmittance of channel 1 for the MS1 meta-atom with different θ_3 values of 30°, 45°, and 60° are illuminated with x-polarized incidence. (b) Simulated transmittance of channel 2 for the MS1 meta-atom with different θ_4 values of 120°, 135°, and 150° are illuminated with y-polarized incidence. (c) Simulated transmittance of channel 1 when the meta-atom of MS2 is illuminated by incident waves with polarization angles of 30°, 45°, and 60°. (d) Transmission amplitude and phase of channel 1 for the meta-atom of MS2 with different $L_1 = 8$ mm, $L_1 = 18.3$ mm, $L_1 = 28.6$ mm under 45° polarized wave illumination. (e) Simulated transmittance of channel 2 when the meta-atom of MS2 is illuminated by incident waves with polarization angles of 120°, 135°, and 150°. (f) Transmission amplitude and phase of channel 2 for the meta-atom of MS2 with different $L_1 = 8$ mm, $L_1 = 18.3$ mm, $L_1 = 28.6$ mm under 135° polarized wave illumination.

the meta-atom design method developed in Sec. II A, the azimuth angles of the four probes for the MS2 meta-atoms are set to $\theta_1 = \arctan(y/x)$, $\theta_2 = \arctan(y/x) + \pi/2$, $\theta_3 = \theta_1 + \pi$, $\theta_4 = \theta_2 + \pi$, respectively. It is worth noting that probe 1 (probe 2) and probe 3 (probe 4) are 180° symmetrical, which only results in a constant 180° phase difference between the incident and transmitted waves, while their polarization angles remain unchanged.

Figure 3(c) shows the simulated transmittance of channel 1 when the meta-atom of MS2 is illuminated by 30°, 45°, and 60° polarized incident waves. The values of θ_1 are 30°, 45°, and 60°, while $\theta_3 = 210°, 225°, 240°$, respectively. The transmittances are higher than 0.9 at 7.8 GHz.

To illustrate the modulation of the transmitted waves in channel 1 by L_1, the amplitude and phase of the transmitted waves are depicted in Fig. 3(d) when a MS2 meta-atom with different L_1 is excited by 45° polarized incident waves. Here, subscripts 1, 2, and 3 denote three cases where $L_1 = 8$ mm, $L_1 = 18.3$ mm, and $L_1 = 28.6$ mm, while the other geometric parameters of the meta-atoms remain unchanged. We can observe that when the L_1 difference is $\Delta L_1 = 10.3$ mm $= \lambda_g/2$ and $\Delta L_1 = 20.5$ mm $= \lambda_g$, the corresponding phase difference is 180° and 360°, respectively. At the same time, the transmission amplitude in all cases remains higher than 0.9 at 7.8 GHz. Figure 3(e) shows the simulated transmittance of channel 2, where it can be observed that the transmittance at 7.8 GHz is still higher than 0.9. The transmission phase and transmission amplitude of the MS2 meta-atom with different $L_2 = 8$ mm, 18.3 mm, 28.6 mm under 135° polarization wave illumination are also shown in Fig. 3(f). The transmission phase varies in a 360° range and the amplitude for these cases is above 0.9 at 7.8 GHz. The two channels do not influence each other since their polarizations are orthogonal. Therefore, the designed dual-channel MS2 meta-atom can efficiently modulate the transmission phase of two independent channels without changing the amplitude and polarization of the transmitted waves.

C. Design of metasurfaces for tightly focusing CVBs

In this section we analyze how the two dual-channel transmissive metasurfaces can be employed to generate and modulate different CVBs independently. The meta-atoms of MS1 and MS2 are arranged according to the polarization states of the RPB and APB. Both metasurfaces with a similar size of 300×300 mm^2 and containing 30×30 meta-atoms are used.

The regular-polygon-like focus and 2D lateral displacement of the focal spot are realized in different focal planes through the two channels, respectively. To achieve these goals, a high NA lens and a phase DOE is required to adjust the phase distributions of the different CVBs. Figure 4 illustrates the schematic diagram of MS2 tightly focusing a RPB through channel 1. Hence, MS2 can be regarded as a multifunctional device that integrates the function of a lens as well as that of a phase DOE providing an additional phase distribution to the incident CVB. According to Richards-Wolf theory [41], the electric field in the focal plane ($z = f_1$) with an RPB focused by a high NA lens can be expressed as

$$E(x, y, z = f_1) = [E_x \; E_y \; E_z]$$
$$= -\frac{ikf_1}{2\pi} \int_0^{2\pi} \int_0^{\beta} \sin(\alpha)\cos^{1/2}(\alpha)l(\alpha)T(\alpha, \phi)$$
$$\times \exp ik \sin\alpha (x \sin\alpha + y\cos\alpha)$$
$$\times [\cos(\alpha)\cos(\phi) \; \cos(\alpha)\sin(\phi) \; \sin(\alpha)]d\phi d\alpha, \quad (5)$$

where x and y are Cartesian coordinates in the focal plane, and E_x, E_y, and E_z are the components of the E-fields in the x, y and, z directions, respectively. Here $k = 2\pi/\lambda_0$ is the wave number in free space, f_1 represents the focal length of the lens and satisfies the condition $r = f_1 * \sin\alpha$, where α is the half convergence angle with a maximum value $\beta = \sin(\mathrm{NA}/n)$. The refractive index of the medium between the focal plane and the lens is expressed as n, and ϕ and r are the azimuth angle and radial coordinates on the DOE, respectively. If the location of the MS2 meta-atom is (x, y), its azimuth angle can be expressed as $\phi = \arctan(y/x)$. Since the dimension of the MS2 is 300×300 mm^2, a suitable aperture stop radius is $R_1 = 150$ mm. $T(\alpha, \phi)$ is the transmittance function of the DOE, which is used to characterize the modulation of the incident waves by the DOE. $l(\alpha)$ describes the phase and amplitude distributions of the incident beam and a plane wave with $l(\alpha) = 1$ is assumed to be the illuminating source. In addition, NA $= 0.75$, $n = 1$, and $f_1 = 200$ mm are adopted in this design. To achieve a regular-polygon-like focus with N edges through channel 1 under RPB excitation, the MS2 used for RPB phase modulation is divided into N ($N = 3, 4, 5, \ldots$) equal sector-shaped subareas to produce an N focal point array in the focal plane, where each sector-shaped subarea has a central angle of $2\pi/N$. The phase distributions of the mth subarea [42] is

$$
\begin{aligned}
P_m(x, y) = -k\sin\alpha r_1 [&\cos(\phi_m + \pi/2)\cos(\arctan(y/x)) \\
&+ \sin(\phi_m + \pi/2)\sin(\arctan(y/x))] \\
m = (1, 2, \ldots, N), \quad &(6)
\end{aligned}
$$

where m ($m = 1, 2, \ldots, N$) is the index of each subarea, r_1 is the distance from each focus spot to the origin of the focal plane, ϕ_m is the angle bisector of the mth subarea, which can be expressed as $\phi_m = (2m - 1)\pi/N$. As a demonstration, $N = 4$ and $r_1 = 1.5\lambda$ are used in Eq. (6) to design the DOE for regular-polygon-like focusing. Since the designed meta-atom has a period P, the phase distributions of the DOE and metasurfaces are discretized using $P = 10$ mm. The phase of the focusing lens of channel 1 is described using

$$
P_{f1}(x, y) = 2\pi/\lambda(\sqrt{x^2 + y^2 + f_1^2} - f_1). \quad (7)
$$

Then, the total phase distribution $P_{t1}(x, y)$ on MS2 for channel 1 is obtained through the superposition of the DOE phase and focusing lens phase, and can be expressed as

$$
P_{t1}(x, y) = P_{f1}(x, y) + P_m(x, y). \quad (8)
$$

To investigate the modulation effect of the DOE on the focal field distribution, the phase distribution of the MS2 and the corresponding E-field intensity distributions in the focal plane $z = 200$ mm when $r_1 = \lambda$, $r_1 = 1.5\lambda$, $r_1 = 2\lambda$
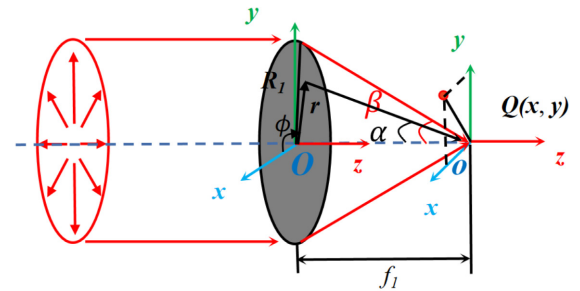
FIG. 4. Schematic diagram of tightly focused RPB beam with DOE modulation for channel 1.

at 7.8 GHz are plotted in Fig. 5. As r_1 increases, the four spots gradually move away from the center of the focal plane. A diamond-shaped focal spot is formed if $r_1 = \lambda$ while a regular-polygon-like focus is obtained when $r_1 = 1.5\lambda$. When r_1 is further increased to 2λ, the E-field in the focal plane becomes a focal array with four focal spots. In summary, by changing the value of r_1, a variety of focal fields can be obtained using DOEs with different phase distributions. Furthermore, a 2D lateral displacement of the focal spot is realized through channel 2 when MS2 is excited by an APB. Figure 6 shows the schematic diagram for calculating the focused field with lateral displacement. The transmitted field E_t is the vector angular spectrum of the focal field E under a tightly focused condition. The E-field in the focal region then can be written as [43]

$$
\begin{aligned}
E(x, y, z = f_1) = &-\frac{ikf_1}{2\pi}\int_0^{2\pi}\int_0^\beta P(\alpha)E_t(\alpha, \phi) \\
&\times \exp(-ik\sqrt{x^2 + y^2}\sin\alpha[(\tan(y/x))^{-1} \\
&- \phi])\exp(ikz\cos\alpha)\sin\alpha\, d\phi\, d\alpha, \quad (9)
\end{aligned}
$$

where A is a constant related to the focal length and wavelength, (x, y, z) are the coordinates of the focal region, and $P(\alpha) = 1$ is the pupil function for incident waves adopted in our design. The focal field E at any point (x, y) in the focal region can be further written as the Fourier transform (FT) of the weighted field E_t under the high NA lens focusing condition [42]. Based on the shift theorem of FT, a 2D lateral displacement $(\Delta x, \Delta y)$ of the focal spot can be achieved by introducing a specific phase shift to the incident field. The phase-only expression controlling the 2D lateral displacement of the focal spot in channel 2 of MS2 can be expressed as

$$
P_{2d}(x, y) = \frac{2\pi}{\lambda}\frac{\mathrm{NA}}{R_1 n}(x\Delta x + y\Delta y). \quad (10)
$$

Here the aperture stop radius is set to $R_1 = 150$ mm. In addition, the phase profile $P_{f2}(x, y)$ for focusing the APB in channel 2 is obtained from Eq. (7), corresponding to a
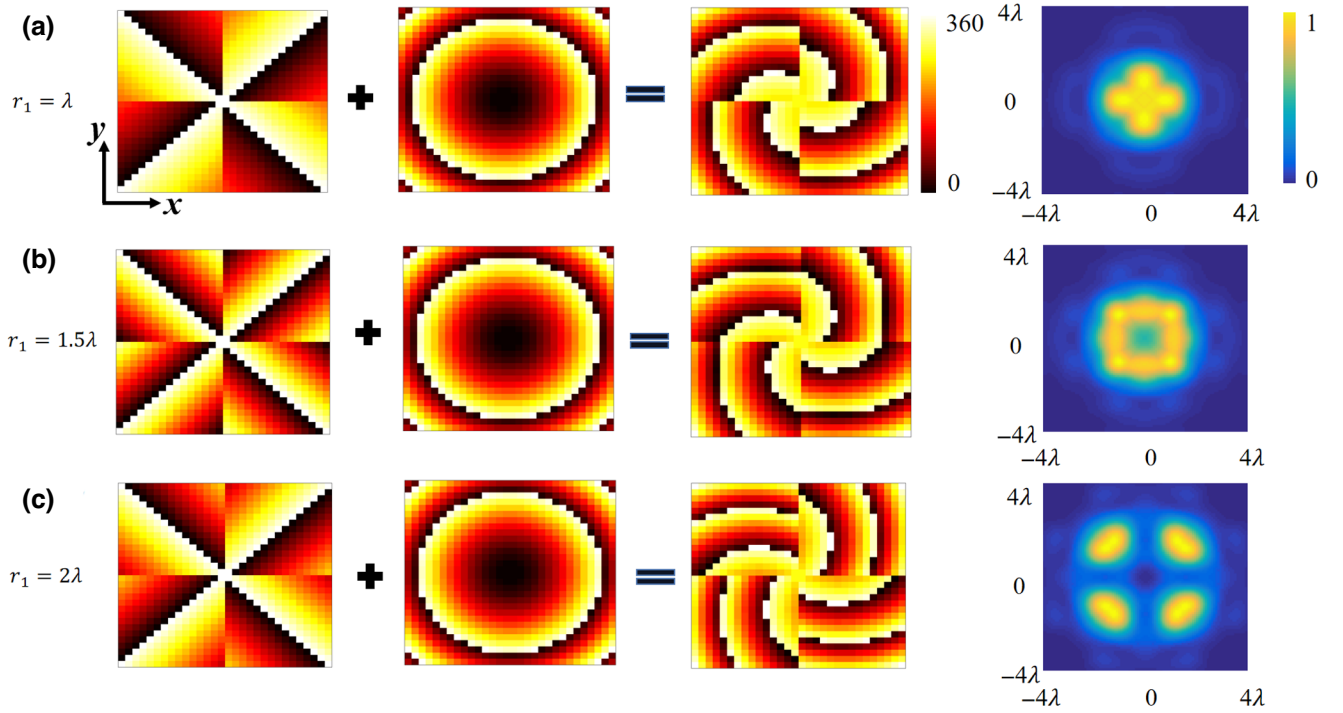
FIG. 5. Phase distributions of the DOEs and lens combined to achieve the total phase distribution for RPB modulation for channel 1 of MS2, and the E-field intensity distribution in the focal plane $z = 200$ mm: (a) $r_1 = \lambda$, (b) $r_1 = 1.5\lambda$, and (c) $r_1 = 2\lambda$.

NA of 1 and a focal length $f_1 = 150$ mm. The total phase distribution on MS2 for a modulating APB is

$$P_{t2}(x,y) = P_{f2}(x,y) + P_{2d}(x,y). \qquad (11)$$

The E-field in the focal plane ($z = f_1$) for a tightly focused APB is calculated using Eq. (9). Figure 7(a) shows the calculated focusing phase for the lens with NA $= 1$ and the E-field intensity in the focal plane. Since only a focusing phase is applied and there is no DOE modulation ($\Delta x = \Delta y = 0$) in channel 2, a doughnut-shaped E-field pattern of the focused APB is observed at the center of the focal plane. Then, the phase distribution of the DOE for channel 2 obtained from Eq. (10) is applied when $\Delta x = \lambda$ and $\Delta y = -\lambda$. As shown in Fig. 7(b), the phase distribution of the DOE is similar to a phase gradient, which is widely used for beam deflection in metasurface designs. The phase distribution for APB modulation is equal to the sum of the phase on the DOE and the focusing phase. In addition, the E-field intensity in the case of a tightly focused APB with DOE modulation is shown in Fig. 7(b), and it can be observed that the center of the focal spot moves from $(0, 0)$ to $(\lambda, -\lambda)$. Thus, a position-controlled tight focal spot is achieved via the additional phase modulation.

III. RESULTS AND DISCUSSION

MS1 is simulated to verify the design of the dual-channel transmissive metasurface for RPB and APB generation. The simulated E-field vectors of different channels in the plane $z = 0$ mm at 7.8 GHz with x- and y-polarized wave incidences are shown in Figs. 8(a) and 8(e), respectively, and MS1 is placed in the $z = -50$ mm plane in simulation. Note that the vector distributions of the E-field are consistent with the polarization states of the ideal RPB and APB. In addition, since the designed meta-atom can efficiently achieve linear polarization conversion and the E-field intensity distribution is uniform in the xoy plane, as illustrated by the normalized magnitudes of E_x and E_y of the RPB and the APB in Figs. 8(b) and 8(c) and Figs. 8(f) and 8(g), respectively. To realize the tight focusing of different CVBs, the RPB and APB generated using MS1 are used to illuminate
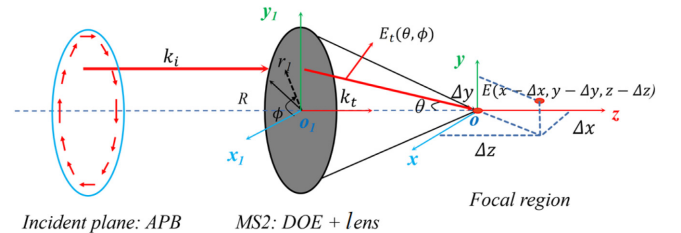

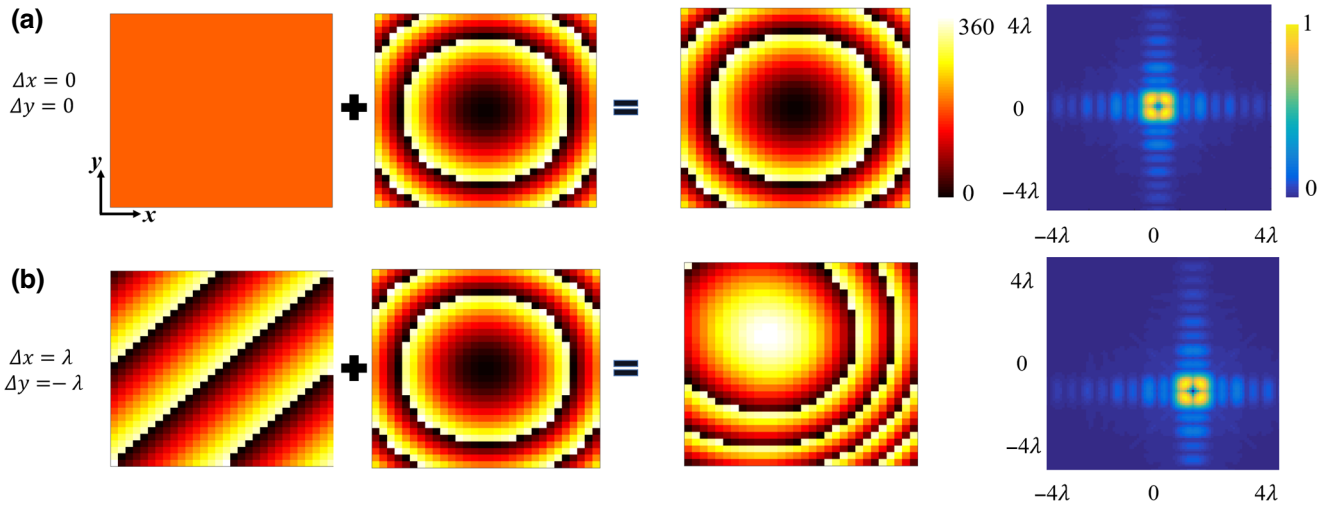FIG. 6. Schematic diagram for calculating the focused field with lateral displacement.

FIG. 7.   Phase distribution of DOEs and lenses for channel 2, total phase distribution for APB modulation for channel 2 of MS2, and the E-field intensity distribution in the focal plane $z = 150$ mm. (a) $\Delta x = 0$, $\Delta y = 0$ and (b) $\Delta x = \lambda$, $\Delta y = -\lambda$.

MS2, which is capable of independently modulating their phases. In the simulations, MS1 and MS2 are cascaded at a distance of 50 mm since the wave front between MS1 and MS2 needs to be redistributed during propagation, which ensures that MS2 can be excited by the ideal RPB or APB generated by MS1. Figs. 8(d) and 8(h) depict the simulated E-field distribution in the focal planes $z = 200$ mm and $z = 150$ mm when MS2 is illuminated by the RPB and APB through channel 1 and channel 2 at 7.8 GHz, respectively. To realize the regular-polygon-like focus when MS2 is excited by the RPB, the value of r_1 in Eq. (9) should be chosen judiciously. As shown in Fig. 8(d), when $r_1 = 1.5\lambda$, a regular-polygon-like focus is obtained in consistency with the previous analysis, and the distance from the four focal spots to the center of the focal plane is 1.5λ. Furthermore, the tightly focused
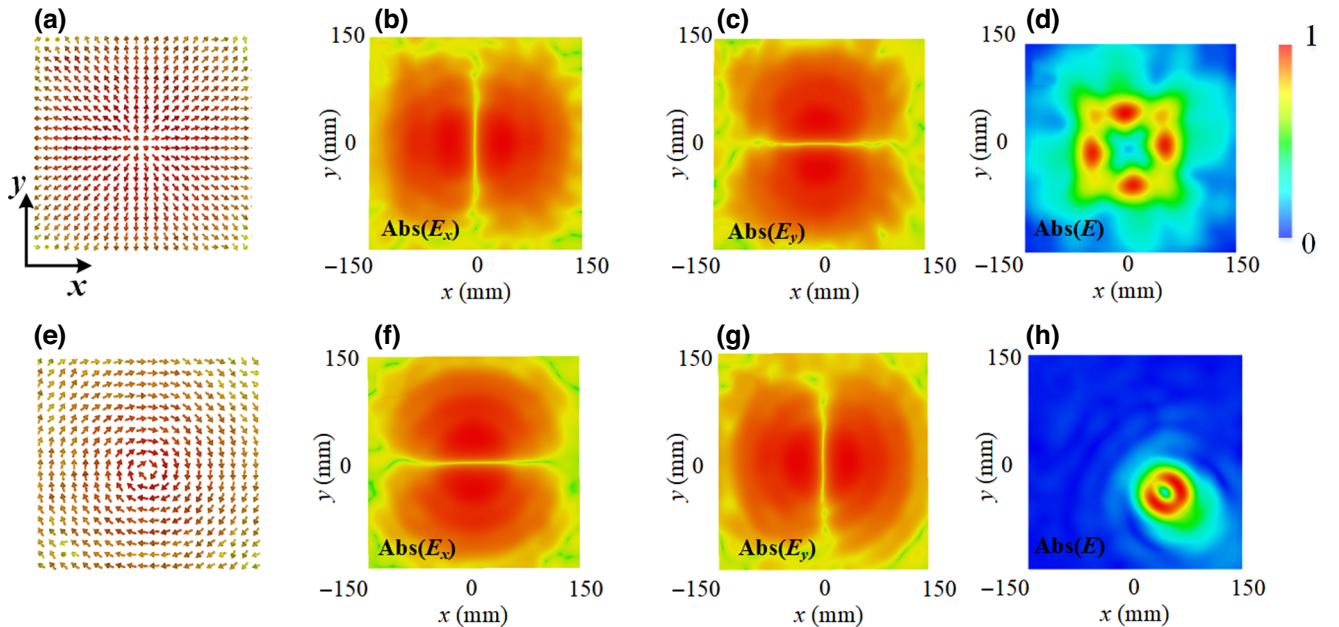

FIG. 8.   (a) Simulated E-field vector for channel 1 of MS1 under x-polarized wave incidence in the $z = 0$ mm plane. (b) Simulated normalized magnitude of E_x of RPB. (c) Simulated normalized magnitude of E_x of RPB. (d) Simulated normalized magnitude of E-field in plane $z = 200$ mm when MS2 is illuminated by an RPB in channel 1. (e) Simulated E-field vector for channel 2 of MS1 under y-polarized wave incidence in plane $z = 0$ mm. (f) Simulated normalized magnitude of E_x of the APB. (g) Simulated normalized magnitude of E_x of the APB. (h) Simulated normalized magnitude of E-fields in the $z = 150$ mm plane when MS2 is illuminated by an APB in channel 2.
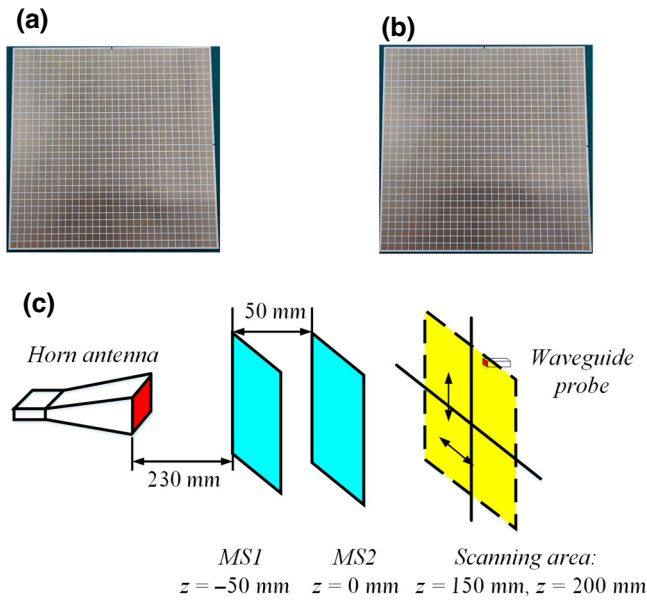
FIG. 9. Photograph of (a) MS1 and (b) MS2. (c) A 2D schematic of the experimental setup.

spot of the APB is realized in the focal plane $z = 150$ mm with a 2D lateral displacement $(\lambda, -\lambda)$, as shown in Fig. 8(h). The simulated results in Figs. 8(d) and 8(h) agree well with the calculated fields in Figs. 5(b) and 7(b).

To experimentally demonstrate the design approach, MS1 and MS2 with dimensions of 300×300 mm^2 are

fabricated using the conventional printed circuit board technique, as shown in Figs. 9(a) and 9(b). The measurements are performed in a microwave anechoic chamber to avoid environmental interference. A field scanning system as depicted in Fig. 9(c) is employed to measure the E-field in different planes. A horn antenna acting as the excitation source is placed 230 mm behind MS1. A waveguide probe is used as the detector to measure the E-field distribution in the scanning planes $z = 200$ mm and $z = 150$ mm. The excitation antenna and the waveguide probe are both connected to a vector network analyzer (Agilent E8363B) via coaxial cables. The detection probe is moved over a scanning area of 300×300 mm^2 with a step resolution of 7.5 mm to record the x and y components of the E-field. To validate the performance of MS1, the E-filed is first measured in the plane $z = 0$ mm under x- and y-polarized wave illuminations. Figures 10(a) and 10(b) show the measured E_x and E_y when MS1 is illuminated by an x-polarized wave through channel 1. The measurement results are consistent with the simulation results of Figs. 8(b) and 8(c). Under y-polarized wave incidence, the measured E_x and E_y in Figs. 10(d) and 10(e) are also consistent with the simulation results in Figs. 8(f) and 8(g). As depicted in Fig. 9(c), MS2 is placed at a distance of 50 mm in front of MS1 to tailor the phase of the APB and the RPB independently. As shown in Figs. 10(c) and 10(f), the two dual-channel transmissive cascaded metasurfaces can achieve a regular-polygon-like focus and a focal spot with a 2D lateral displacement in the focal planes $z = 200$ mm
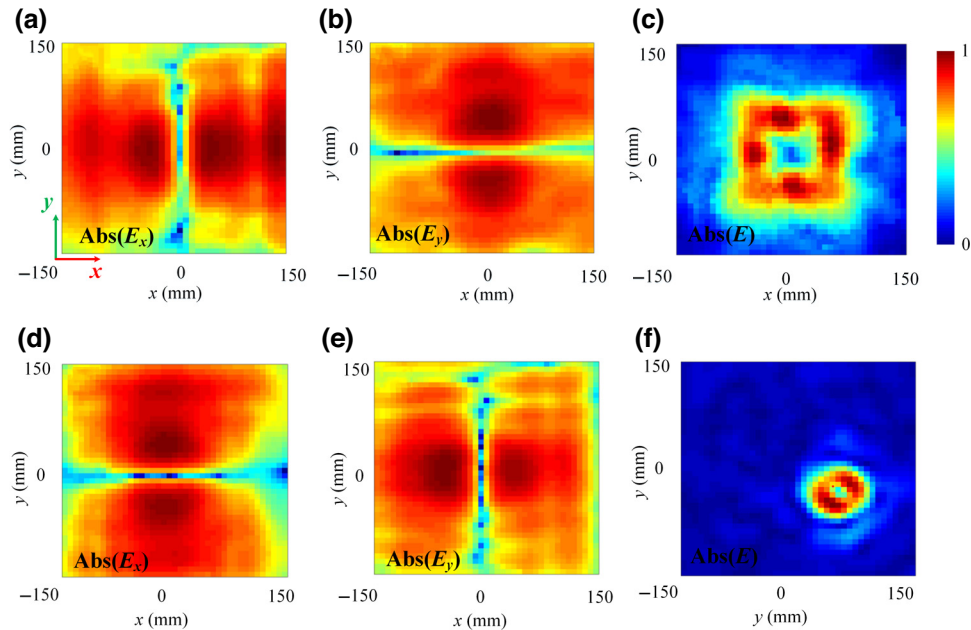

FIG. 10. Measured normalized magnitude of (a) E_x and E_y in the plane $z = 0$ mm under x-polarized wave illumination of channel 1 of MS1. (c) Measured normalized magnitude of E-field in focal plane $z = 200$ mm under RPB illumination of channel 1 of MS2. Measured normalized magnitude of (d) E_x and (e) E_y in plane $z = 0$ mm under y-polarized wave illumination of channel 2 of MS1. (f) Measured normalized magnitude of E-field in focal plane $z = 150$ mm under APB illumination of channel 2 of MS2.

and $z = 150$ mm, respectively. Ignoring the manufacturing and measurement errors, the simulation and measurement results are in good qualitative agreement. Thus, different focal fields can be realized from the two cascaded dual-channel metasurfaces under illumination of x- and y-polarized waves through different channels.

IV. CONCLUSION

In this work we first design a dual-channel coupling-propagation-decoupling meta-atom to control both the phase and polarization of the transmitted waves independently through a change of only two geometric parameters. Then we propose a dual-channel transmissive metasurface in the microwave range based on the designed meta-atoms for CVB generation. Under the x- and y-polarized waves incidence, the polarization of the output wave in channel 1 and channel 2 becomes radial and angular, respectively. We also design a second metasurface, which can be seen as a dual-channel device that combines a lens and a DOE, to independently control the phase of the RPB and APB and achieve tight focus of the vector beams. The two dual-channel metasurfaces are cascaded to realize a regular polygonlike flat-top focus and lateral displacement of the focal spot in different focal planes under x- and y-polarized wave excitations, respectively. A good agreement between theoretical, simulation, and experimental results is obtained. Compared with reported studies, the innovation of our design resides in the independent phase and polarization modulation of different vector beams, which greatly simplifies the design process. Furthermore, our method has great potential in medical applications such as microwave hyperthermia treatment since it can be used to concentrate EM wave energy effectively and generate various complex focal fields in specific areas. As a potential application, our design can be used to treat tumors on the surface or very close to the surface, and the operating frequency can be lowered to treat tumors located deep in the tissue as our design approach can be transposed to other frequencies.

[1] Q. W. Zhan, Cylindrical vector beams from mathematical concepts to applications, Adv. Opt. Photonics **1**, 1 (2009).

[2] D. G. Hall, Vector-beam solutions of Maxwell's wave equation, Opt. Lett. **21**, 911 (1996).

[3] G. Bautista, M. J. Huttunen, J. Mäkitalo, J. M. Kontio, J. Simonen, and M. Kauranen, Second-harmonic generation imaging of metal nano-objects with cylindrical vector beams, Nano Lett. **12**, 63207 (2012).

[4] C. J. Min, Z. Shen, J. F. Shen, Y. Q. Zhang, H. Fang, G. H. Yuan, L. P. Du, S. W. Zhu, T. Lei, and X. C. Yuan, Focused plasmonic trapping of metallic particles, Nat. Commun. **4**, 63207 (2013).

[5] M. Giovanni, A. N. Thien, L. Jonathan, A. N. Daniel, and R. A. Robert, Using the nonseparability of vector beams to encode information for optical communication, Opt. Lett. **40**, 4887 (2015).

[6] J. R. Brian and C. T. Kimani, Optical trapping with π-phase cylindrical vector beams, New J. Phys. **12**, 073012 (2010).

[7] H. F. Wang, L. P. Shi, B. Lukyanchuk, C. Sheppard, and C. T. Chong, Creation of a needle of longitudinally polarized light in vacuum using binary optics, Nat. Photonics **2**, 501 (2008).

[8] L. W. Zhu, R. Yang, D. W. Zhang, J. J. Yu, and J. N. Chen, Dynamic three-dimensional multifocal spots in high numerical-aperture objectives, Opt. Express **25**, 24756 (2017).

[9] X. L. Wang, B. W. Zhu, Y. X. Dong, S. Wang, Z. Q. Zhu, F. Bo, and X. P. Li, Generation of equilateral-polygon-like flat-top focus by tightly focusing radially polarized beams superposed with off-axis vortex arrays, Opt. Express **22**, 26844 (2017).

[10] D. Pohl, Operation of a ruby laser in the purely transverse electric mode TE01, Appl. Phys. Lett. **20**, 266 (1972).

[11] S. Ngcobo, I. Litvin, L. Burger, and A. Forbes, A digital laser for on-demand laser modes, Nat. Commun. **4**, 2289 (2013).

[12] P. Li, X. H. Fan, D. J. Wu, X. Y. Guo, Y. Li, S. Liu, and J. L. Zhao, Shaping vector fields in three dimensions by random Fourier phase-only encoding, Opt. Express **27**, 30009 (2019).

[13] G. F. Wu, F. Wang, and Y. J. Cai, Generation and self-healing of a radially polarized Bessel-Gauss beam, Phys. Rev. A **89**, 043807 (2014).

[14] Z. Bomzon, G. Biener, V. Kleiner, and E. Hasman, Radially and azimuthally polarized beams generated by space-variant dielectric subwavelength gratings, Opt. Lett. **27**, 285 (2002).

[15] H. Chen, J. J. Hao, B. F. Zhang, J. Xu, J. P. Ding, and H. T. Wang, Generation of vector beam with space-variant distribution of both polarization and phase, Opt. Lett. **36**, 3179 (2011).

[16] N. F. Yu, P. Genevet, M. A. F. Kats, J. Tetienne Aieta, F. Capasso, and Z. Gaburro, Light propagation with phase discontinuities: Generalized laws of reflection and refraction, Science **334**, 333 (2011).

[17] Z. M. Lin, X. W. Li, R. Z. Zhao, X. Song, Y. T. Wang, and L. L. Huang, High-efficiency Bessel beam array generation by Huygens metasurfaces, Nanophotonics **8**, 1079 (2019).

[18] H. Y. Shi, L. Y. Wang, X. M. Chen, A. X. Zhang, and Z. Xu, Generation of a microwave beam with both orbital and spin angular momenta using a transparent metasurface, J. Appl. Phys. **126**, 063108 (2019).

[19] G. X. Zheng, H. Muhlenbernd, M. Kenney, G. X. Li, T. Zentgraf, and S. Zhang, Metasurface holograms reaching 80% efficiency, Nat. Nanotechnol. **10**, 308 (2015).

[20] H. X. Xu, G. W. Hu, L. Han, M. H. Jiang, Y. J. Huang, Y. Li, X. M. Yang, X. H. Ling, L. Z. Chen, J. L. Zhao, and C. W. Qiu, Chirality-assisted high-efficiency metasurfaces with independent control of phase, amplitude, and polarization, Adv. Opt. Mater. **4**, 1801479 (2019).

[21] E. Arbabi, A. Arbabi, S. M. Kamali, Y. Horie, and A. Faraon, Multiwavelength polarization-insensitive lenses based on dielectric metasurfaces with meta-molecules, Optica **3**, 628 (2016).

[22] R. Z. Zhao, B. Sain, Q. S. Wei, C. C. Tang, X. W. Li, T. Weiss, L. L. Huang, Y. T. Wang, and T. Zentgraf, Multichannel vectorial holographic display and encryption, Light-Sci. Appl. **7,** 9 (2018).

[23] J. Lin, P. Genevet, M. A. Kats, N. Antoniou, and F. Capasso, Nanostructured holograms for broadband manipulation of vector beams, Nano Lett. **13,** 4269 (2018).

[24] J. T. Heiden, F. Ding, J. Linnet, Y. Q. Yang, J. Beermann, and S. I. Bozhevolnyi, Gap-surface plasmon metasurfaces for broadband circular-to-linear polarization conversion and vector vortex beam generation, Adv. Opt. Mater. **7,** 1801414 (2019).

[25] J. Han, Y. Intaravanne, A. Ma, R. X. Wang, S. T. Li, Z. C. Li, S. Q. Chen, J. Li, and X. Z. Chen, Optical metasurfaces for generation and superposition of optical ring vortex beams, Laser Photonics Rev. **14,** 2000146 (2019).

[26] Y. J. Bao, J. C. Ni, and C. W. Qiu, A minimalist single-layer metasurface for arbitrary and full control of vector vortex beams, Adv. Mater. **32,** 1905659 (2020).

[27] F. Y. Yue, D. D. Wen, J. T. Xin, B. D. Gerardot, J. Li, and X. Z. Chen, Vector vortex beam generation with a single plasmonic metasurfac, ACS Photonics **3,** 1558 (2016).

[28] J. Y. Guo, X. K. Wang, J. W. He, H. Zhao, S. F. Feng, P. Han, J. S. Ye, W. F. Sun, G. H. Situ, and Y. Zhang, Generation of radial polarized Lorentz beam with single layer metasurface, Adv. Opt. Mater. **6,** 1700925 (2018).

[29] Z. P. Zhuang, R. Chen, Z. B. Fan, X. N. Pang, and J. W. Dong, High focusing efficiency in subdiffraction focusing metalens, Nanophotonics **8,** 1279 (2019).

[30] R. Z. Zuo, W. W. Liu, H. Cheng, S. Q. Chen, and J. G. Tian, Breaking the diffraction limit with radially polarized light based on dielectric metalenses, Adv. Opt. Mater. **6,** 1800795 (2018).

[31] F. Zhang, H. L. Yu, J. W. Fang, M. Zhang, S. C. Chen, J. Wang, A. G. He, and J. Y. Chen, Efficient generation and tight focusing of radially polarized beam from linearly polarized beam with all-dielectric metasurface, Opt. Express **24,** 6656 (2016).

[32] F. Ding, Y. T. Chen, Y. Q. Yang, and S. I. Bozhevolnyi, Multifunctional metamirrors for broadband focused vector-beam generation, Adv. Opt. Mater. **7,** 1900724 (2019).

[33] H. Y. Zheng, M. Z. He, Y. Zhou, I. I. Kravchenko, J. D. Caldwell, and J. G. Valentine, Compound meta-optics for complete and loss-less field control, ACS Nano **9,** 15100 (2022).

[34] R. S. Xie, X. D. Bai, J. Liu, X. Wang, Y. N. Zheng, Z. Gu, H. L. Zhang, C. B. Jing, J. Ding, and J. H. Chu, Dual-channel geometric meta-holograms with complex-amplitude modulation based on bi-spectral single-substrate-layer meta-atoms, Opt. Express **30,** 42850 (2022).

[35] P. Wust, B. Hildebrandt, Y. Sreenivasa, B. Rau, J. Gellermann, H. Riess, R. Felix, and P. M. Schlag, Hyperthermia in combined treatment of cancer, Lancet Oncol. **3,** 487 (2002).

[36] O. Nielsen, M. Horsman, and J. Overgaard, A future for hyperthermia in cancer treatment, Eur. J. Cancer **37,** 1587 (2001).

[37] Y. H. Tao and G. Wang, Conformal hyperthermia of superficial tumor with left-handed metamaterial lens applicator, IEEE Trans. Biomed. Eng. **59,** 3525 (2012).

[38] M. Kowalski, B. Behnia, A. Webb, and J. M. Jin, Optimization of electromagnetic phased-arrays for hyperthermia via magnetic resonance temperature estimation, IEEE Trans. Biomed. Eng. **49,** 1229 (2002).

[39] C. Pfeiffer and A. Grbic, Controlling Vector Bessel Beams with Metasurfaces, Phys. Rev. Appl. **2,** 044012 (2014).

[40] L. D. Shao, D. J. Zhang, J. Liu, J. Zhang, Z. F. Li, X. Wang, and W. R. Zhu, Single-layer noninterleaved metasurface for arbitrary vector beam conversion in triple bands, ACS Appl. Electron. Mater. **4,** 443 (2022).

[41] B. RICHARDS and E. WOLF, Electromagnetic diffraction in optical systems, II. Structure of the image field in an aplanatic syste, Proc. R. Soc. London, A **253,** 358 (1959).

[42] S. S. Gong, T. Zhang, and M. J. Li, Achievement of regular-polygon-like focus through tightly focusing phase modulated radially polarized beam, Optik **242,** 166865 (2021).

[43] M. Leutenegger, R. Rao, R. A. Leitgeb, and T. Lasser, Fast focus field calculations, Opt. Express **14,** 11277 (2016).